Advanced Composites and Hybrid Materials (2023) 6:2
https://doi.org/10.1007/s42114-022-00579-z

RESEARCH

Ultra-hydrophilic nanofiltration membranes fabricated via punching in the HTO nanosheets

Fangyi Yao[1] · Wenxiong Zhang[2] · Dengwei Hu[3] · Sen Li[4] · Xingang Kong[5] · Shinobu Uemura[1] · Takafumi Kusunose[1] · Qi Feng[1]

Received: 29 August 2022 / Revised: 21 October 2022 / Accepted: 7 November 2022 / Published online: 30 November 2022

Abstract

Nanoporous layered titanate (HTO) nanosheet membranes were fabricated via restacking nanoporous HTO nanosheets on a hydrophilic polytetrafluoroethylene (PTFE) filter substrate. Nanoporous HTO nanosheets were prepared by exfoliating a nanoporous HTO that was obtained by selectively dissolving $BaTiO_3$ (BT) nanoparticles in a mesocrystalline BT/HTO nanocomposite in an HCl solution. The BT/HTO nanocomposites were synthesized by the solvothermal treatment of HTO platelike particles in a $Ba(OH)_2$ solution. The pore size of the nanoporous HTO nanosheet membrane was controlled by the BT nanoparticle size in the BT/HTO nanocomposite. Meanwhile, the size of the BT nanoparticle was controllable by the solvothermal synthesis conditions of the BT/HTO nanocomposite, including the reaction temperature, Ba/Ti mole ratio, and solvent in the reaction system. Furthermore, we designed a self-adjusting membrane thickness process (SAMTP) to efficiently fabricate nanoporous HTO nanosheet membranes on the PTFE substrate. The rejection of solutes with different sizes and water permeance capacities demonstrated that the nanoporous HTO nanosheet membranes fabricated by the SAMTP possessed size-controlled nanopores with uniform size in the range of 1.5–100 nm, uniform nanometer-scale thicknesses, excellent hydrophilicity, high water permeance, and good durability. Thus, the fabricated nanoporous HTO nanosheet membranes would be excellent candidates for water treatment and molecule separation.

Keywords Inorganic nanoporous membrane · Hydrophilic separation membrane · Nanoporous layered titanate nanosheet · Water treatment

1 Introduction

According to a prediction of the United Nations, two-thirds of the world's population will be living in water-stressed conditions by 2050 [1]. As a result, much research attention has been focused on the worldwide water shortage crisis [2]. Membrane separation technology is an efficient technique for water purification due to its high efficiency, ease of operation, and low energy consumption [3–5]. The pore size is the most important parameter of porous membranes. Based on the pore size, porous membranes can be classified as microfiltration (MF), ultrafiltration (UF), nanofiltration (NF), and reverse osmosis (RO) membranes [6–8]. NF and RO membranes with smallest pore sizes in the range of 0.5–2 nm are mainly used to separate small molecules and ions [9, 10]. The NF and RO membranes, which are typically commercially available, are polymer-based products and have advantages such as superior chemical resistance, oxidation resistance, and ease of fabrication. Undoubtedly, polymeric NF and RO membranes are currently in the forefront of separation and water treatment membranes dues to their well establishment and outstanding track records [11]. One of the critical issues in the currently use of polymeric NF and RO membranes in water treatment is the trade-off relationship between permeability and selectivity, as well as membrane fouling resistance and scaling [12].

✉ Qi Feng
feng.qi@kagawa-u.ac.jp

1 Department of Advanced Materials Science, Faculty of Engineering and Design, Kagawa University, 2217-20 Hayashi-Cho, Takamatsu-Shi 761-0396, Japan

2 Institute for Solid State Physics, The University of Tokyo, Sayo, Hyogo 679-5148, Japan

3 College of Chemistry and Chemical Engineering, Baoji University of Arts and Sciences, 1-Hi-Tech Avenue, Baoji, Shaanxi 721013, People's Republic of China

4 Materials Science and Engineering, Southern University of Science and Technology, Nanshan, 1088 Xueyuan Avenue, Shenzhen, Guangdong 518055, China

5 School of Materials Science and Engineering, Shaanxi University of Science and Technology, Weiyang, Xi'an, Shaanxi 710021, People's Republic of China

Inorganic membranes possess high hydrophilicity, which can improve permeability and selectivity of the membranes and reduce fouling. Furthermore, good mechanical strength is also expected for the inorganic membranes [13]. Some inorganic membranes, including ceramic [14], zeolite [15], metal organic framework (MOF) [16, 17], and nanocarbon-based membranes, have been developed [18, 19]. Both theoretical calculations and experiment performances of the inorganic-based nanoporous membranes have been conducted in separation applications [20–22]. Graphene, a typical two-dimensional nanocarbon material with a single-atom thickness, is a promising material for next-generation separation membranes, due to its very thin nanosheet morphology, excellent flexibility, mechanical strength, and thermal and chemical stabilities [23]. Several theoretical studies have been carried out, while limited numbers of the experimental studies have been conducted on porous graphene membranes for applications in water treatment. Usually, pristine graphene is a non-porous nanosheet without permeability for water or ions [24, 25]. Therefore, it has become a challenge to open nanopores in graphene nanosheets. O'Hern et al. have reported studies on single-layer nanoporous graphene membranes fabricated by using ion irradiation, chemical etching, and O_2 plasma treatment of intact graphene nanosheets [26, 27]. The experimental studies have demonstrated the exceptional mechanical strength, fast water transport, and negligible thickness of nanoporous graphene membranes in water desalination [28]. However, these experimental studies were limited to millimeter-scale membranes because currently used processes cannot provide large-size, single-layer, nanoporous graphene membranes concisely [29].

Vacuum filtration is a traditional and straightforward process applied to fabricate large-scale membranes using two-dimensional nanomaterials. However, membranes with uniform thicknesses at the nanometer scale are difficult to fabricate. Moreover, one of the problems with vacuum filtration is time-consuming [30]. Multi-layer graphene membranes with micrometer-scale thicknesses have been fabricated by this process using non-porous graphene nanosheets [31]. Water molecules or small organic molecules pass through the multi-layer, non-porous graphene membrane from the interlayer spaces of the multilayered stacked graphene nanosheets, extending the migration distance of the molecules required to pass through the membrane and reducing the permeance performance [32]. Moreover, this technique can easily introduce defects in the fabricated membranes [33]. Compared with graphene-based membranes, metal oxide nanosheets exhibit excellent hydrophilicity, which can improve the water permeance for high-performance nanoporous membranes. The vacuum filtration technique was also employed to fabricate multi-layer nanosheet membranes using non-porous metal oxide nanosheets. The fabricated metal oxide nanosheet membranes exhibited relatively large thicknesses of over 500 nm, leading to a decline in the water permeance [34]. A layer-by-layer (LBL) deposition strategy is a relatively cost-effective technique for the fabrication of multi-layer metal-oxide nanosheet thin films with nanometer-scale thicknesses, where charged nanosheet membrane thickness can be obtained by controlling the number of sequential adsorption steps [35]. However, this process has not been used to fabricate the porous membranes of metal oxide nanosheets.

It is well known that a good NF or RO membrane should have a high water permeance, selectively rejection rate, applicable in basic, acidic, or other harsh environments [36]. It is predicted that if a nanoporous metal oxide nanosheet were available, high-performance nanoporous membranes could be obtained by stacking the nanoporous nanosheets. However, to the best of our knowledge, such nanoporous metal oxide nanosheets and their nanoporous membranes have not been reported yet. Layered titanate with a lepidocrocite-like structure $H_{1.07}Ti_{1.73}O_4{\cdot}nH_2O$ (HTO) exhibits excellent ion-exchange properties, good chemical stability, and hydrophilicity, which could be easily exfoliated into nanosheets by intercalation of an organic amine into the interlayer space. This provides potential applications for nanomaterials and as a precursor for the soft chemical syntheses of functional nanomaterials [37].

Herein, we describe a facile and unique approach to fabricate nanoporous membrane using nanoporous HTO nanosheets, as shown in Fig. 1. A soft chemical process was designed for the synthesis of the nanoporous layered titanate nanosheets, including the synthesis of mesocrystalline $BaTiO_3$/HTO (BT/HTO) nanocomposites, by partially transforming HTO into BT nanoparticles, selectively removing BT nanoparticles in the BT/HTO nanocomposite by an acid treatment to obtain nanoporous HTO particles, and exfoliating the nanoporous HTO particles into nanoporous HTO nanosheets with a thickness of 1 nm per layer. Furthermore, we fabricated a nanoporous HTO nanosheet membrane for water treatment and filtration by restacking the exfoliated nanoporous HTO nanosheets. For the first time, we developed a smart and effective process, namely, a self-adjusting membrane thickness process (SAMTP), for the fabrication of nanoporous membranes. The results of the size rejection measurements indicated that the nanoporous HTO nanosheet membranes fabricated by this SAMTP possessed uniform size-controlled nanopores in a range of 1.5–100 nm, uniform nanometer-scale thicknesses, excellent hydrophilicity, high water permeance, and good durability. These membranes can be applied as excellent low energy–consuming nanoporous membranes for water treatment and molecule separation. These nanoporous HTO nanosheet membranes could usher in a new era of inorganic nanoporous membrane materials.

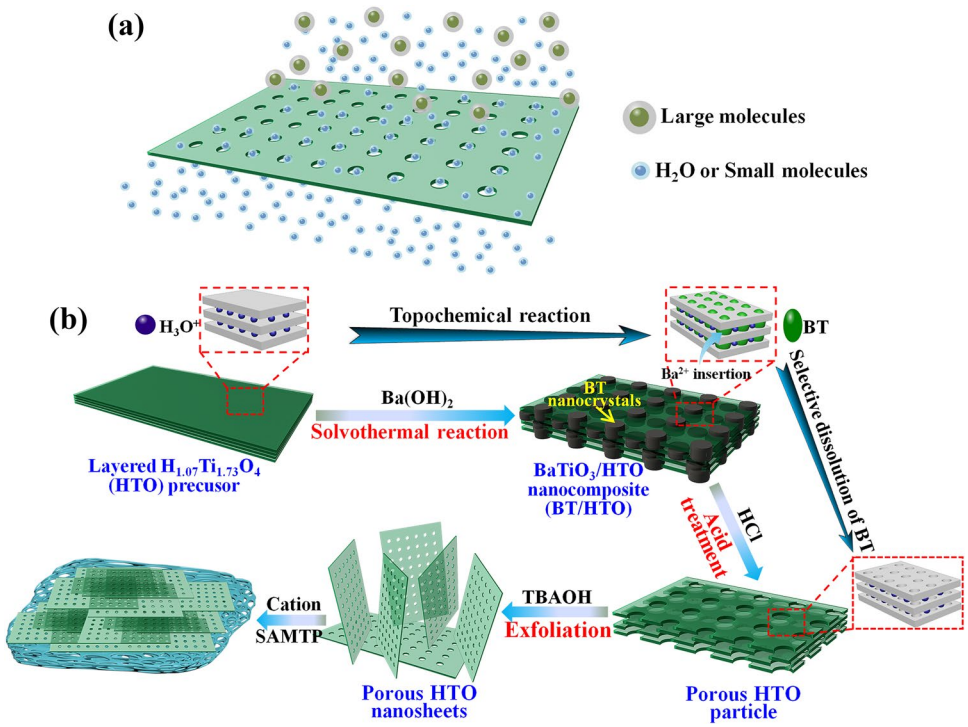

Fig. 1 **a** Schematic illustrations of size exclusion separation mechanism of nanoporous HTO membrane and **b** fabrication process of nanoporous HTO membrane for efficient molecular separation

2 Experimental

2.1 Preparation of nanoporous layered titanate $H_{1.07}Ti_{1.73}O_4{\cdot}nH_2O$ (HTO) particles and BT/HTO nanocomposites

The layered titanate $H_{1.07}Ti_{1.73}O_4{\cdot}nH_2O$ (HTO) powder precursor was prepared by the acid treatment of $K_{0.8}Ti_{1.73}Li_{0.27}O_4$ (KTLO) powder that was synthesized by the hydrothermal process, as reported in our previous study [38]. The X-ray diffraction (XRD) patterns and scanning electron microscopy (SEM) images of the KTLO and HTO are shown in Figs. S1 and S2, respectively. Both KTLO and HTO possessed typical platelike particle morphologies. In the synthesis process of the $BaTiO_3/H_{1.07}Ti_{1.73}O_4{\cdot}nH_2O$ (BT/HTO) nanocomposite, the HTO precursor (0.165 g) and a desired amount of $Ba(OH)_2{\cdot}8H_2O$ were solvothermally treated in 30 mL of different solvents under continuous stirring conditions at a desired temperature for 12 h. Water, a water–ethanol mixture (volume ratio = 1:1), and ethanol were used as solvents. Subsequently, the obtained samples were washed with distilled water and dried at room temperature (RT) to obtain the BT/HTO nanocomposites. The synthesized BT/HTO samples were designated as BT/HTO-X–Y-Z, where X, Y, and Z represent the Ba/Ti mole ratio (0.4, 0.5 and 0.75), reaction temperature (80, 100 and 125 °C), and solvent (water: W, water–ethanol: W/E, and ethanol: E) in the reaction system, respectively. To obtain the nanoporous HTO (P-HTO) particles, a synthesized BT/HTO-X–Y-Z sample (0.5 g) was treated in an HCl solution (100 mL) with a desired concentration under stirring at RT for 12 h to dissolve BT nanocrystals in the BT/HTO sample. After washing with distilled water and drying at RT, the P-HTO samples were obtained, which were labeled as P-HTO-X–Y-Z.

2.2 Preparations of HTO nanosheets and P-HTO nanosheet solutions

A layered HTO or P-HTO sample (1 g) was exfoliated in a 0.016 $mol{\cdot}L^{-1}$ tetrabutylammonium hydroxide (TBAOH) solution (200 mL) while stirring at RT for a desired time. After resting for at least 1 week, the supernatant colloidal solution was used as the HTO or P-HTO nanosheet solution. The obtained HTO and P-HTO nanosheets were named HTO-NS and P-HTO-NS-X–Y-Z, respectively.

2.3 Fabrication of HTO and P-HTO nanosheet membranes

A hydrophilic polytetrafluoroethylene (PTFE) membrane filter (JGWP04700 Millipore Membrane Filter, pore size: 0.20 μm) was chosen as the porous substrate for the fabrication of the nanosheet membrane owing to its high mechanical strength. The PTFE porous substrate was ultrasonically cleaned in a 50% ethanol solution for 1 h to remove organics adsorbed on the surface before use. The nanosheet membrane was fabricated by depositing the nanosheets on the

surface of the PTFE porous substrate via a self-adjusting membrane thickness process (SAMTP), as illustrated in Scheme 1A. Briefly, the PTFE porous substrate was clamped in the middle of a home-made glass U-tube cell with an inner diameter of 10 mm and an effective area of 0.785 cm^{-2} for water transport. The exfoliated nanosheet solution and an electrolytic solution ($CaCl_2$, NaCl, or HNO_3) were filled with equivalent volumes (20 mL) in the two compartments of the glass U-tube cell. Then, the negatively charged nanosheets could react with cations of the electrolyte solution on the surface of the porous PTFE substrate to form a nanosheet membrane. During the fabrication process, the nanosheet solution compartment side was stirred to ensure the homogeneous reaction near the surface of the porous PTFE substrate. The fabricated HTO and P-HTO nanosheet membranes were named M-HTO and M-P-HTO-X–Y-Z, respectively.

2.4 Measurement of salt rejection and water permeance

A home-made glass U-tube cell with an inner diameter of 10 mm separated by nanosheet membrane was used to verify the salt rejection and water-flux performances of the fabricated nanosheet membranes, as depicted in Scheme 1B. Distilled water (20 mL) and a 0.5 mol·L^{-1} NaCl solution (20 mL) were added to either compartment of the U-tube cell. After 12 h, the NaCl concentration on the distilled water side was measured using an ion conductivity meter (East Asian DKK CM-41X). The salt rejection efficiency R (%) was calculated as follows:

$$R = \frac{C_0 - C_x}{C_0} \times 100\% \quad (1)$$

where C_0 is the initial concentration of the NaCl solution, and C_x is the NaCl concentration on the distilled water side after 12 h.

To measurement the water flux for an NaCl solution, a 0.5 mol·L^{-1} NaCl solution (20 mL) was added on one compartment of the U-tube cell, and the other compartment was empty. After a desired time (t, h), the volume (V, L) of water that had passed through the nanosheet membrane was measured on the empty side. The water flux J (L/m^{-2}·h^{-1}) was calculated using as follows:

$$J = \frac{V}{A \times t} \quad (2)$$

where A is effective membrane area (m^2).

The rejection efficiencies for methylene blue (MB) and polydopamine (PD) and the water fluxes for MB and PD solutions were measured by a similar method to that used for the NaCl solution with 100-ppm MB and 500-ppm PD solutions, respectively. The concentrations of the MB and PD solutions were determined using ultraviolet–visible (UV–vis) spectroscopy. The PD solution was prepared as follows: 1 mL of Tris HCl (pH = 8.5) was added into 99 mL of distilled water. Next, 50 mg of 3-hydroxytyramine hydrochloride (> 98%) was dissolved in 99 mL of Tris HCl solution and stirred for 5 min at ambient temperature to obtain a light brown homogeneous PD solution. The particle size of PD was measured using a zeta potential and particle size analyzer (Photal ELSZ-2 KG).

2.5 Physical property characterization

The crystal phases of the powder samples were investigated using a powder X-ray diffractometer (Shimadzu, XRD-6100) with Cu $K\alpha$ ($\lambda = 0.15418$ nm) radiation. The particle morphologies were observed using field-emission scanning electron microscopy (FE-SEM, Hitachi, S-900). Transmission electron microscopy (TEM) observations and selected-area electron diffraction (SAED) were performed on a JEOL Model JEM-3010 system at 300 kV, and the samples were supported on a Cu microgrid. Raman spectra were collected using a Renishaw InVia Raman microscope with a laser operating at 532 nm. The laser power at the sample was estimated to be 1%, and the nominal laser spot size was 10 µm. The Brunauer–Emmett–Teller (BET) surface areas were measured using a computer-controlled automatic gas sorption system (Quantachrome NOVA 4200e), and the

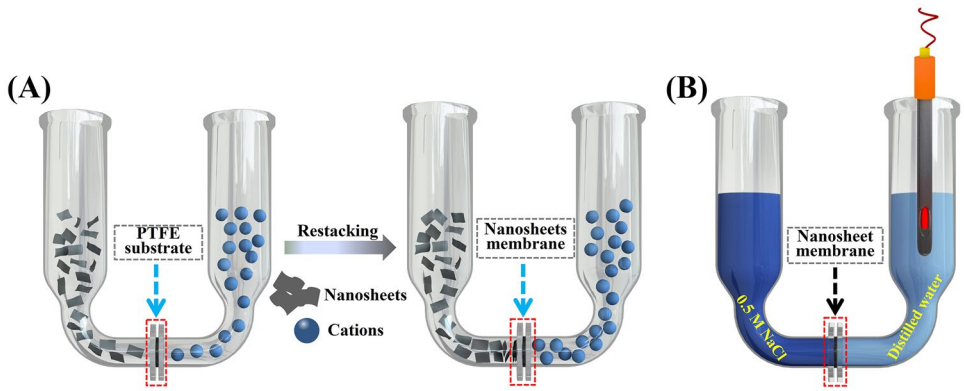

Scheme 1 **A** Self-adjusting membrane thickness process (SAMTP) for fabrication of nanosheet membrane via nanosheet restacking. **B** Measurement method of salt rejection performance

samples were degassed at 573 K (300 °C) for 2 h before the measurements. The hydrophilicity of the membranes was characterized using an automatic water contact angle meter (CA-VP, FACE, Kyowa Interface Science, Japan). A membrane sample with a diameter of 25 mm was attached onto a glass slide, and 3.0 μL of distilled water was dropped onto the air-side surface of the membrane at room temperature. At least five measurement results were averaged to obtain an average value.

3 Results and discussion

3.1 Synthesis of BT/HTO nanocomposite

Layered titanate $H_{1.07}Ti_{1.73}O_4{\cdot}nH_2O$ (HTO) crystals with lepidocrocite-like (γ-FeOOH) layered structures were used as the precursor to prepare nanoporous HTO nanosheets by a soft chemical process. First, a $BaTiO_3$/HTO (BT/HTO) nanocomposite was prepared by solvothermal treatment of the HTO precursor in a $Ba(OH)_2$ solution. Figure 2A presents the XRD patterns of the HTO precursor and the BT/HTO nanocomposites obtained by solvothermal treatments of HTO crystals in $Ba(OH)_2$ solutions with a Ba/Ti molar ratio of 0.5 in water (W), water–ethanol (W/E), and ethanol (E) solvents at 125 °C for 12 h. The HTO sample produced an XRD pattern of the lepidocrocite-like (γ-FeOOH) layered orthorhombic structure with a basal spacing of 0.92 nm (Fig. 2A(a)). After the solvothermal reaction in a $Ba(OH)_2$ solution, except for the unreacted HTO phase, the formation of the cubic BT phase (JCPDS File No. 74–1964) was observed in the water–ethanol and ethanol solvents (Fig. 2A(c) and (d)). That indicated that the HTO precursor was partially transformed into the BT phase. The diffraction peaks of the BT phase were not observed clearly in the sample prepared in the water solvent, whereas the diffraction peak intensity of the HTO phase decreased, suggesting the formation of the BT phase with a low crystallinity or amorphous BT phase. BT/HTO-0.5–125-W/E exhibited a higher intensity and smaller full width at half maximum (FWHM) of the diffraction peaks of the BT phase than those of the BT/HTO-0.5–125-E, suggesting that the number and crystal sizes of BT nanocrystals were larger in this sample. The basal spacing of the unreacted HTO layered phase decreased

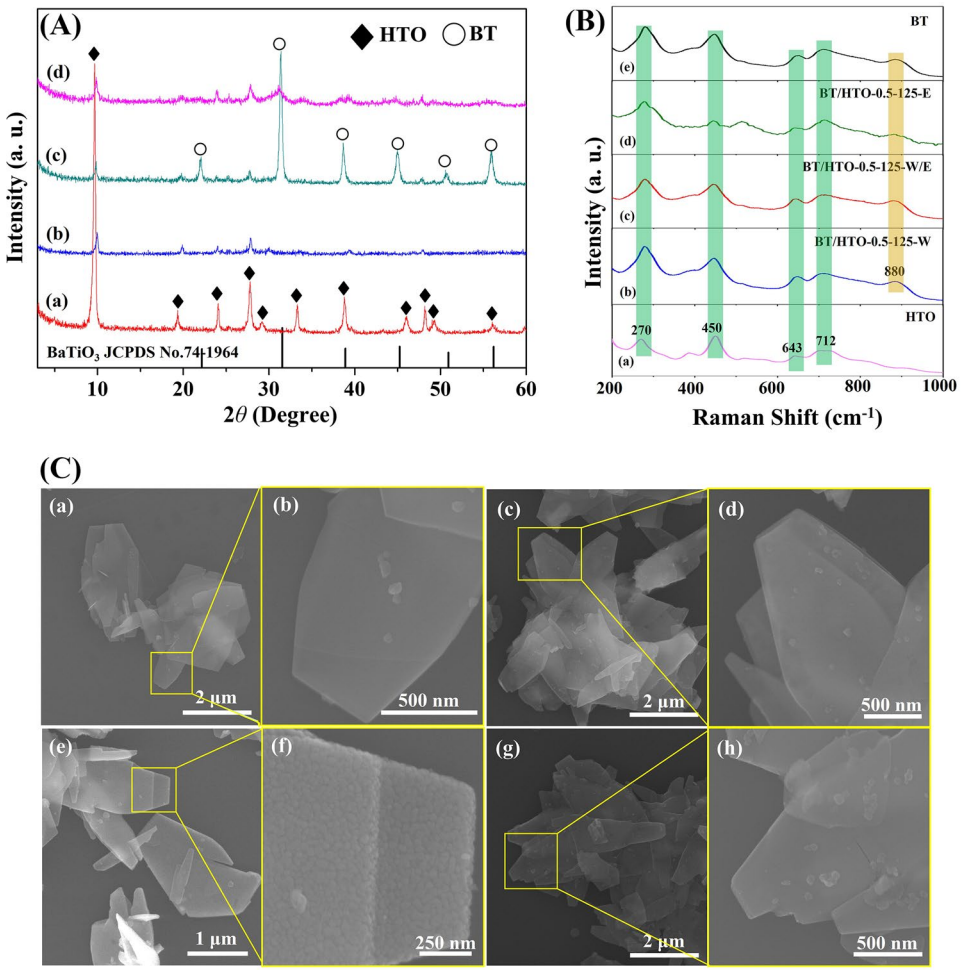

Fig. 2 **A** X-ray diffraction (XRD) patterns of (**a**) $H_{1.07}Ti_{1.73}O_4{\cdot}nH_2O$ (HTO) precursor, (**b**) BT/HTO-0.5–125-W, (**c**) BT/HTO-0.5–125-W/E, and (**d**) BT/HTO-0.5–125-E nanocomposites. **B** Raman spectra of (**a**) HTO precursor, (**b**) BT/HTO-0.5–125-W, (**c**) BT/HTO-0.5–125-W/E, (**d**) BT/HTO-0.5–125-E, and (**e**) BT samples. **C** Field-emission scanning electron microscopy (FE-SEM) images of (**a**, **b**) HTO precursor, (**c**, **d**) BT/HTO-0.5–125-W, (**e**, **f**) BT/HTO-0.5–125-W/E, and (**g**, **h**) BT/HTO-0.5–125-E nanocomposites

slightly from 0.92 nm of the HTO precursor to 0.90 nm, illustrating that the H_3O^+ ions were exchanged by Ba^{2+} ions in the interlayer spaces of the HTO precursor. This result verified the insertion of Ba^{2+} into the interlayer spaces in the BT/HTO nanocomposite formation process.

The above results showed that the solvent was one of the significant factors affecting the BT formation reaction. The reactivity of $Ba(OH)_2$ and HTO had a strong correlation with the polarity of the reaction solvent and $Ba(OH)_2$ concentration. In the water–ethanol (W/E) mixed solvent system, the polarity of the solvent increased with increasing water content. Generally, the increase in the solvent polarity will enhance the reactivity between $Ba(OH)_2$ and the HTO precursor, which promotes the formation of the BT phase. Therefore, the water–ethanol mixed solvent exhibited a higher reactivity for the formation of the BT phase than the ethanol solvent. However, the increase in the solvent polarity also resulted in the increase in the solubility of $Ba(OH)_2$. The lower reactivity in the water solvent than that in water–ethanol mixed solvent can be explained by the higher solubility of $Ba(OH)_2$ in water and the small amount of $Ba(OH)_2$ added in the reaction system. In the solvothermal reaction system, $Ba(OH)_2$ needed to arrive at an equilibrium concentration for the formation reaction of the BT phase, which consumed some of the $Ba(OH)_2$. The consumed amount of $Ba(OH)_2$ increased as its solubility increased, which reduced the reactivity when the amount of reactant added was small.

Raman spectroscopy was also employed to confirm the formation of the BT phase in the BT/HTO nanocomposites, since it is an effective technique to investigate the formation of BT nanocrystals. The HTO precursor exhibited main vibration bands at around 270, 450, 643, and 712 cm^{-1}, which were assigned to the *A*1(2*TO*) bending vibrations of Ti–OH, asymmetric stretching vibrations of Ti–O-Ti, Ti–O stretching vibrations of TiO_6 octahedra, and symmetric stretching vibrations of Ti–O-Ti, respectively (Fig. 2B(a)) [39–41]. In addition to the vibration bands of the HTO precursor, the BT phase exhibited a specific vibration band at around 880 cm^{-1} (Fig. 2B(e)). This vibration band was assigned to the Ti–O-Ba stretching vibrations of the cubic BT phase caused by the binding of Ba^{2+} to the TiO_6 octahedra [42–44]. The vibration band at around 880 cm^{-1} was observed in all three BT/HTO-0.5–125-Z samples (Fig. 2B(b)–(d)), indicating the formation of the BT phase in these samples. Although the diffraction peaks of BT were not observed in the XRD pattern of BT/HTO-0.5–125-W (Fig. 2A(b)), the Raman spectrum revealed the formation of the BT phase in this sample. The result indicated that Raman spectroscopy was effective for detecting the formation of the amorphous or low-crystallinity BT phase.

The FE-SEM images of the HTO precursor and BT/HTO nanocomposites obtained by solvothermal treatment at 125 °C and Ba/Ti molar ratio of 0.5 are shown in Fig. 2C. The BT/HTO nanocomposites possessed similar platelike particle morphologies to those of the HTO precursors, where the particles had widths of about 1 μm, lengths of about 3 μm, and thicknesses of about 200 nm (Fig. 2C(a) and (b)). Numerous nanoparticles with sizes of about 30–40 nm was observed clearly in the platelike particles of the BT/HTO-0.5–125-W/E (Fig. 2C(f)), which could be indexed to the BT phase, namely, the formation of the BT/HTO nanocomposite. BT nanoparticles were not observed clearly in the BT/HTO-0.5–125-E (Fig. 2C(h)) and BT/HTO-0.5–125-W (Fig. 2C(d)) because their particle sizes were too small. The FE-SEM results were consistent with those of the XRD patterns and Raman spectra, confirming the formation of a low-crystallinity or amorphous BT phase in the BT/HTO-0.5–125-W and BT/HTO-0.5–125-E samples.

To control the BT particle size in the BT/HTO nanocomposite, BT/HTO nanocomposites were synthesized at different solvothermal reaction temperatures. Figures S3 and S4 display the XRD patterns of the products prepared with a Ba/Ti molar ratio of 0.5 in different solvents at 100 and 80 °C. Similar to the case of the reaction at 125 °C, the water–ethanol mixed solvent also exhibited the highest reactivity for the formation of the BT phase at 100 and 80 °C. The formation of the BT phase decreased upon decreasing the solvothermal reaction temperature from 125 to 80 °C. This result implied that the formation of the BT phase was also dependent on the solvothermal reaction temperature. From FE-SEM images, all the BT/HTO nanocomposites retained the platelike particle morphology of the HTO precursor after solvothermal treatment at 100 and 80 °C (Fig. S5). The results further suggested that the BT nanoparticles in the plate-like BT/HTO nanocomposites were formed by a topochemical reaction.

To investigate the influence of the Ba/Ti molar ratio in the solvothermal reaction system on the formation of the BT/HTO nanocomposite, the BT/HTO nanocomposites were also synthesized at Ba/Ti molar ratios of 0.4 and 0.75 and at 125, 100, and 80 °C. Figures S6, S7, and S8 show the XRD patterns of the BT/HTO nanocomposites synthesized at the Ba/Ti molar ratio of 0.4 at 125, 100, and 80 °C in different solvents, respectively. The XRD patterns of the specimens synthesized at the Ba/Ti molar ratio of 0.75 at 125, 100, and 80 °C are shown in Figs. S10, S11, and S12, respectively. The water–ethanol mixed solvent also exhibited the highest reactivity for the formation of the BT phase at Ba/Ti molar ratios of 0.4 and 0.75 at 125, 100, and 80 °C. The formation of the BT phase increased with an increasing Ba/Ti molar ratio in the reaction system. At the Ba/Ti molar ratio of 0.4 in different mixed solvent, no BT peaks were observed at 80 °C, even in the water–ethanol mixed solvent, illustrating that the limiting temperature for the BT phase formation was above 80 °C at a Ba/Ti molar ratio of 0.4 (Fig. S8c). All these BT/HTO nanocomposites retained the platelike

particle morphology of the HTO precursor, as shown in the FE-SEM images (Figs. S9 and S13), suggesting that a topochemical reaction occurred. The above results revealed that particle size and amount of the BT phase in the BT/HTO nanocomposite could be controlled by adjusting the solvothermal reaction conditions, including the reaction temperature, solvent, and Ba/Ti molar ratio.

3.2 Preparation of P-HTO particles

Nanoporous HTO particles (P-HTO) were prepared by dissolution of the BT nanoparticles in the BT/HTO nanocomposites with an HCl solution. Figure 3A shows the XRD patterns of the BT/HTO-0.5–125-W/E nanocomposite before (Fig. 3A(a)) and after acid treatment in 1, 1.5, and 2 mol·L^{-1} HCl solutions for 12 h, respectively. After the acid treatment in a 1 mol·L^{-1} HCl solution (Fig. 3A(b)), the diffraction peak intensity of the BT phase decreased greatly and small amounts of BT residual, while the diffraction peak intensity of the HTO phase increased. After the acid treatment in the 1.5 and 2 mol·L^{-1} HCl solutions, diffraction peaks of the BT phase disappeared completely, suggesting that the BT phase could be dissolved completely in the HCl solution with a concentration higher than 1.5 mol·L^{-1} (Fig. 3A(c)). After the acid treatment in the 2 mol·L^{-1} HCl solution, in addition to peaks of the HTO phase, a characteristic diffraction peak of anatase TiO_2 was also observed (Fig. 3A(d)). Therefore, the dissolution reaction of BT in the HCl solution was as follows:

$$BaTiO_3 + 2H^+ \rightarrow TiO_2 + Ba^{2+} + H_2O \quad (3)$$

The above results revealed that BT nanocrystals possessed a higher solubility than that of HTO in the HCl solution, namely, BT was preferentially dissolved over HTO in the HCl solution. This was a prerequisite for the formation of P-HTO nanoparticles.

Figure 3B presents FE-SEM images of the BT/HTO-0.5–125-W/E before and after acid treatment in the HCl solutions. Many nanoparticles with sizes of 30–40 nm was observed on the plate-like particle surface of the BT/HTO-0.5–125-W/E before the acid treatment (Fig. 3B(a)). After the acid treatment in the 1 mol·L^{-1} HCl solution, some residual BT nanoparticles were observed at the edges of the plate-like particles (Figs. 3B(b) and S14(a)). It is worth noting that the BT nanoparticles disappeared completely and nanopores were observed in the platelike particles after the acid treatment with 1.5 mol·L^{-1} HCl solution (Fig. 3B(c)). Except for the nanopores, some anatase TiO_2 nanoparticles were observed on the plate-like particle surface after 2 mol·L^{-1} HCl solution etching (Figs. 3B(d) and S14(b)). Moreover, the thickness of BT/HTO plate-like particles decreased slightly after the acid treatment due to the dissolution of BT nanocrystals. The results revealed that the dissolution of BT nanoparticles in the BT/HTO nanocomposite was also a topochemical process, where the plate-like particle morphology was well inherited, resulting in nanoporous HTO plate-like particles. Therefore, the 1.5 mol·L^{-1} HCl solution was the optimum condition to selectively remove BT nanoparticles from the BT/HTO nanocomposite via the acid treatment in the subsequent experiments.

Figure 4A shows the XRD patterns of the P-HTO-0.5–125-Z samples obtained by the acid treatment of the BT/HTO-0.5–125-Z nanocomposites in a 1.5 mol·L^{-1} HCl solution. As expected, all the P-HTO-0.5–125-Z samples exhibited one set of diffraction peaks of HTO, implying that the BT phase was removed completely from the BT/HTO nanocomposites by the acid treatment. The dissolution of the BT nanoparticles from the BT/HTO nanocomposites could be confirmed also by the Raman spectrum, as shown in Fig. 4B. The vibration band at around 880 cm^{-1}, corresponding to the Ti–O-Ba stretching vibrations of the cubic BT phase, disappeared after the acid treatment of the BT/HTO-0.5–125-Z

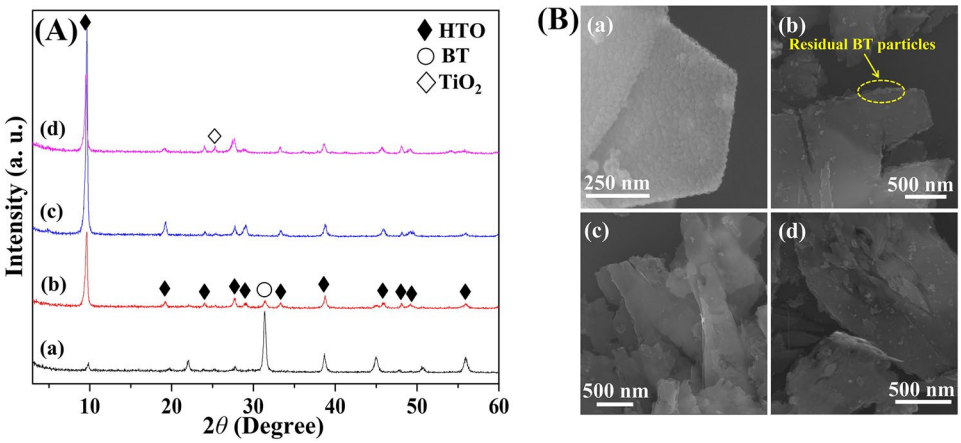

Fig. 3 **A** XRD patterns and **B** FE-SEM images of (**a**) BT/HTO-0.5–125-W/E nanocomposite and P-HTO-0.5–125-W/E samples after acid treatment in (**b**) 1.0, (**c**) 1.5, and (**d**) 2.0 mol·L^{-1} HCl solutions

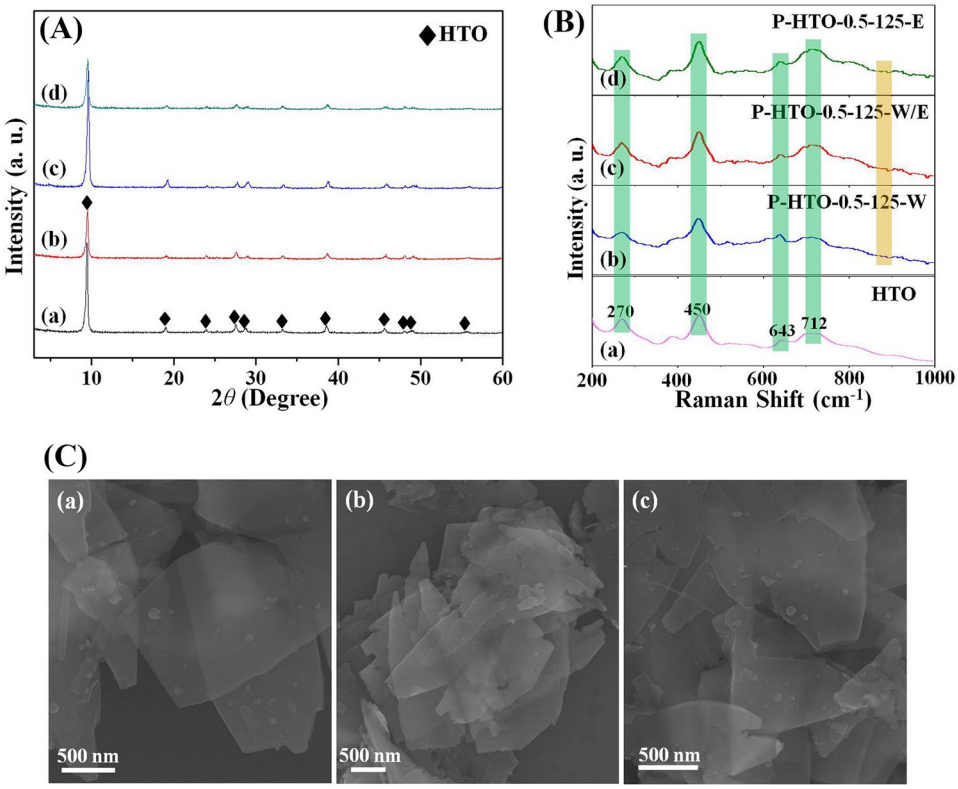

Fig. 4 **A** XRD patterns and **B** Raman spectra of (**a**) HTO precursor, (**b**) P-HTO-0.5–125-W, (**c**) P-HTO-0.5–125-W/E, and (**d**) P-HTO-0.5–125-E particles obtained by acid treatment of BT/HTO-0.5–125-Z nanocomposites in 1.5 mol·L^{-1} HCl solution. **C** FE-SEM images of (**a**) P-HTO-0.5–125-W, (**b**) P-HTO-0.5–125-W/E, and (**c**) P-HTO-0.5–125-E particles

nanocomposites in a 1.5 mol·L^{-1} HCl solution. The acid-treated samples produced Raman spectra corresponding to the HTO precursor. Furthermore, they maintained plate-like particle morphologies similar to that of the HTO precursor, as shown by the FE-SEM images (Fig. 4C). Nanopores were observed in the P-HTO-0.5–125-W/E (Fig. 4C(b)) but not in the P-HTO-0.5–125-W (Fig. 4C(a)) and P-HTO-0.5–125-E (Fig. 4C(c)) due to their small pore sizes. The pore sizes corresponded to the BT nanoparticle sizes in the BT/HTO-0.5–125-Z nanocomposites (Fig. 2).

To further clarify the reaction mechanisms of the formations of the BT/HTO nanocomposite from the HTO precursor and the P-HTO from the BT/HTO nanocomposite, nanostructure analyses on the BT/HTO nanocomposite and P-HTO particles were carried out by employing TEM and SAED. As shown in Fig. 5, the HTO precursor possessed a typical plate-like morphology with a smooth surface and a single-crystalline SAED pattern (Fig. 5a and d). The diffraction spots were assigned to the (002) and (200) facets of the HTO precursor, respectively, revealing that the platelike particles were vertical to the [010] zone-axis (*Z*) of the orthorhombic system. The BT/HTO-0.5–125-W/E nanocomposite inherited this platelike morphology. Notably, there were many spherical nanoparticles with uniform sizes of about 30 nm anchored in the platelike BT/HTO nanocomposite, which corresponded to the BT phase (Fig. 5b). The BT/HTO nanocomposite exhibited two sets of single-crystal-like SAED patterns simultaneously. One was attributed to the perovskite BT phase and the other to the layered HTO phase (Fig. 5e). The result indicated that the HTO and BT phases coexisted in one platelike BT/HTO particle and all of the BT nanocrystals had the same [110] orientation direction, namely, the platelike particle was a mesocrystalline BT/HTO nanocomposite. The uniform BT nanoparticles were also observed in the platelike particles of the BT/HTO-0.5–125-E nanocomposite (Fig. 5c). However, the BT nanoparticle size (3–5 nm) was much smaller than that of the BT/HTO-0.5–125-W/E. The SAED result indicated that BT/HTO-0.5–125-E (Fig. 5f) was also a mesocrystalline BT/HTO nanocomposite similar to the BT/HTO-0.5–125-W/E. The results revealed that the BT nanoparticles in the nanocomposite formed by topochemical reactions of the layered single crystalline HTO precursor.

TEM images and SAED patterns of the acid-treated HTO and P-HTO are shown in Fig. 5g–l. The acid treated HTO particle maintained the original morphology integrity, smooth surface, and layered structure of the HTO precursor (Fig. 5g and j). Remarkably, the acid-treated BT/HTO-0.5–125-W/E nanocomposite possessed a porous platelike architecture, where uniform nanopores with average sizes of 30–40 nm were observed clearly (Fig. 5h). The acid-treated nanocomposite produced the single-crystalline SAED pattern of HTO (Fig. 5k). This indicated the formation of P-HTO single-crystalline platelike particles. The BT

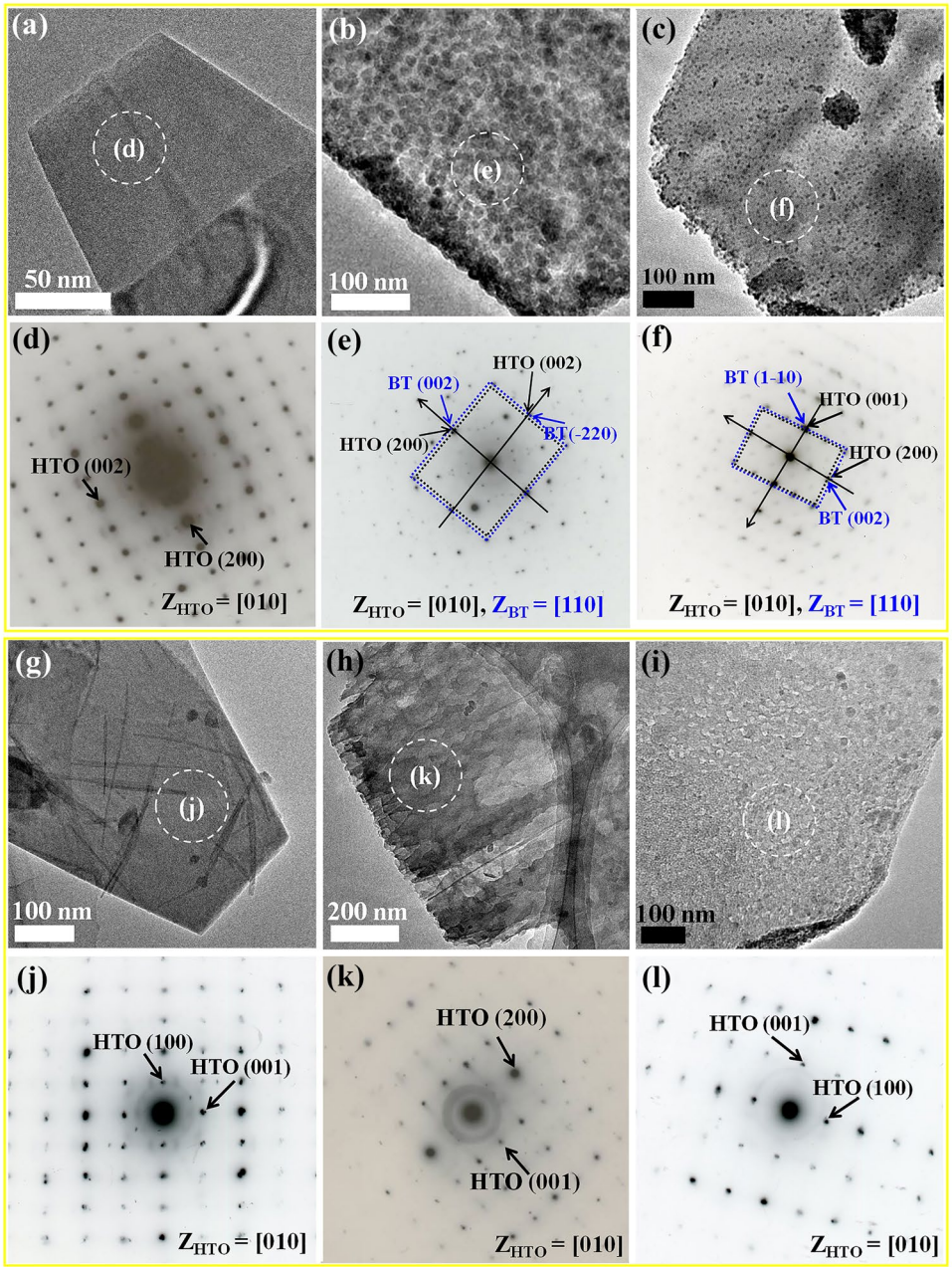

Fig. 5 **a**, **b**, **c**, **g**, **h**, **i** Transmission electron microscopy (TEM) images and **d**, **e**, **f**, **j**, **k**, **l** selected-area electron diffraction (SAED) patterns of **a**, **d** HTO precursor, **b**, **e** BT/HTO-0.5–125-W/E, **c**, **f** BT/HTO-0.5–125-E, **g**, **j** 1.5 mol·L^{-1} HCl acid-treated HTO, **h**, **k** P-HTO-0.5–125-W/E, and **i**, **l** P-HTO-0.5–125-E particles

nanoparticles in the BT/HTO-0.5–125-E nanocomposite were also removed completely by the HCl acid treatment. The P-HTO-0.5–125-E nanocomposite exhibited a porous structural morphology with a homogeneous pore size of about 5–8 nm (Fig. 5i), which corresponded to the BT nanoparticle size in the BT/HTO nanocomposite. As expected, the corresponding SAED pattern in Fig. 5l showed the same single-crystalline diffraction pattern as the HTO precursor. Based on the above results, it was concluded that platelike single-crystalline particles of nanoporous HTO could be obtained by selectively dissolving BT nanoparticles in the mesocrystalline BT/HTO nanocomposites by the acid etching of an HCl solution, and the BT dissolution process was also a topochemical reaction.

The BT/HTO nanocomposites synthesized under other solvothermal conditions, including different temperatures (125, 100, and 80 °C) and different Ba/Ti molar ratios (0.4, 0.5, and 0.75), were acid-treated with a 1.5 mol·L^{-1} HCl solution to prepare nanoporous HTO samples. The XRD results revealed that the BT nanoparticles in these BT/HTO nanocomposites could be removed completely by the acid treatment, like the case of the BT/HTO-0.5–125-Z samples (Figs. S15–S22). The FE-SEM results indicated that the various acid-treated particles retained intact platelike

particle morphologies, resulting in platelike HTO particles with nanoporous morphologies (Figs. S23–S25). The pore size in the P-HTO corresponded to the sizes of the BT nanoparticles in the BT/HTO nanocomposites, which decreased with decreasing solvothermal reaction temperature from 125 to 80 °C for the synthesis of the BT/HTO nanocomposite. The aperture rate of the P-HTO corresponded to the number of BT nanoparticles formed in the BT/HTO nanocomposite, which increased with increasing Ba/Ti molar ratio from 0.4 to 0.75 in the solvothermal reaction system for the synthesis of the nanocomposite. The results further verified that the dissolution reaction of the BT nanoparticles by the acid treatment was a topochemical process. Therefore, the pore sizes in the P-HTO particles could be facilely controlled by a solvothermal reaction temperature and the reaction solvent, while the aperture rate could be controlled by the molar ratio of Ba/Ti in the solvothermal reaction system.

The nanoporous structure of the P-HTO was further investigated by surface area measurements. The BET surface area results of the HTO precursor, BT/HTO-0.5–125-Z nanocomposites, and P-HTO-0.5–125-Z samples are summarized in Table 1. The HTO precursor possessed a BET surface area of 20.1 $m^2 \cdot g^{-1}$, while the BT/HTO nanocomposites possessed slightly lower surface areas. However, the BET surface areas were 32.0, 29.3, and 48.6 $m^2 \cdot g^{-1}$ for the P-HTO-0.5–125-W, P-HTO-0.5–125-W/E, and P-HTO-0.5–125-E samples, respectively, which were larger than those of the non-porous HTO precursor and BT/HTO nanocomposites. The increased surface area for the P-HTO was attributed to the formation of the nanopores in the platelike particles. The largest BET surface area of the P-HTO-0.5–125-E may be due to the formation of the smallest nanopores in the P-HTO-0.5–125-W/E.

3.3 Exfoliation reaction of P-HTO particles to P-HTO nanosheets (P-HTO-NS)

It has been reported that layered HTO can be exfoliated to nanosheets by intercalating organic amines into the interlayer spaces [45]. Therefore, supposing the nanoporous HTO (P-HTO) sample could be exfoliated to nanosheets, nanoporous HTO nanosheets (P-HTO-NS) could be obtained. We prepared P-HTO-NS by the exfoliation of P-HTO particles. When the P-HTO particles were treated in a TBAOH solution, a colloidal suspension was formed, which exhibited a Tyndall phenomenon, as shown in Fig. S26. This suggested that exfoliation of the layered structure of the P-HTO to its nanosheets occurred by intercalating TBA^+ ions into the interlayer spaces, similar to process for normal non-porous HTO particles. The colloidal suspension showed good stability, being stable at RT for more than several months.

Figure 6 shows the TEM images of the exfoliated P-HTO-NS-0.5–125-Z nanosheets. The P-HTO-NS possessed a nanoporous nanosheet-like architecture with a uniform pore size. The results confirmed that the layered structure of the P-HTO was successfully exfoliated to the P-HTO-NS in the TBAOH solution. The pore sizes of the P-HTO-NS-0.5–125-W, P-HTO-NS-0.5–125-W/E, and P-HTO-NS-0.5–125-E nanosheets were about 25–30, 40–50, and 5–10 nm, respectively, which corresponded to the pore sizes in the P-HTO particles as well as the BT particle sizes in the BT/HTO nanocomposites. The aperture rate of the P-HTO-NS decreased with decreasing solvothermal reaction temperature for the synthesis of the BT/HTO nanocomposites (Fig. S27). The lower solvothermal reaction temperature resulted in a less uniform pore size. The BT/HTO nanocomposite synthesized in the ethanol solvent yielded the minimum, uniform pore size. The pore sizes of the nanosheets were dependent on the solvothermal synthesis conditions of the BT/HTO nanocomposite.

Table 1 Surface area measurement results of HTO, BT/HTO-0.5–125-Z, and P-HTO-0.5–125-Z

Sample	BET surface area (m^2/g)	Change of surface area (%)
HTO	20.1	0
BT/HTO-125-W	16.2	−19.4%
BT/HTO-125-W/E	19.3	−4.0%
BT/HTO-125-E	19.1	−5.0%
P-HTO-0.5–125-W	32.0	59.2%
P-HTO-0.5–125-W/E	29.3	45.8%
P-HTO-0.5–125-E	48.6	141.8%

3.4 Formation mechanism of P-HTO-NS

Based on the demonstrated results, the formation mechanism for the P-HTO-NS is proposed, as schematically illustrated in Fig. 1. In the $Ba(OH)_2$ solution, first, Ba^{2+} ions intercalated into the interlayer spaces of the layered structure of the HTO particles and further reacted partially with the TiO_6 octahedral layers to form BT nanoparticles inside the platelike particles of HTO under solvothermal conditions. The solvothermal reaction resulted in the formation of the mesocrystalline BT/HTO nanocomposite, where BT nanoparticles were anchored in the platelike particles of HTO (Fig. 5b and c). All the BT nanoparticles presented the same crystal-axis orientation due to the BT nanoparticles being formed by an in situ topochemical reaction [46, 47]. The topochemical reaction maintained the platelike particle morphology and resulted in a uniform particle size of the BT nanoparticles in the platelike BT/HTO nanocomposites. When the BT/HTO nanocomposite was treated in the HCl solution, the H^+ ions intercalated into the HTO interlayer spaces of the layered structure and sequentially reacted with the

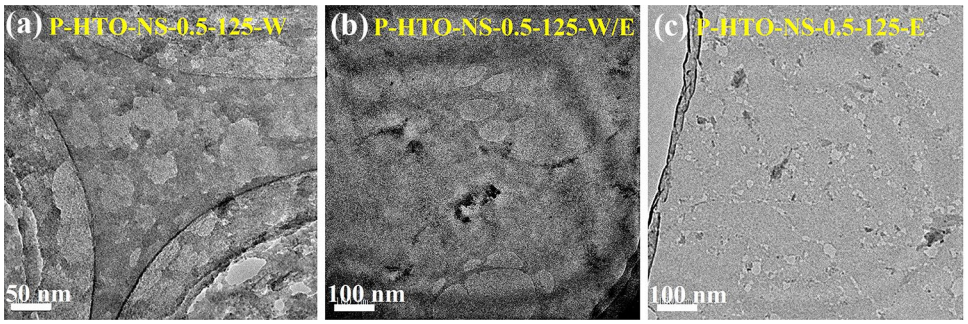

Fig. 6 TEM images of P-HTO-NS. **a** P-HTO-NS-125-W. **b** P-HTO-NS-125-W/E. **c** P-HTO-NS-125-E

BT nanoparticles. The BT nanoparticles were selectively dissolved by the acid treatment because of the higher solubility of BT nanoparticles than that of HTO in the HCl solution. The topochemical dissolution of the BT nanoparticles in the platelike particles of the BT/HTO nanocomposite resulted in the nanoporous platelike particle morphology of the HTO. Therefore, the pore sizes in the P-HTO platelike particles were dependent on the sizes of the formed BT nanoparticles.

In the exfoliation reaction of the P-HTO particles, TBA^+ ions intercalated into the interlayer space of the layered structure by an ion-exchange reaction with H^+ ions. The TBA^+ intercalation reaction caused the increased basal spacing of the HTO layered structure. Meanwhile, a large amount of water entered the interlayer space, forming a swollen phase. Finally, P-HTO particles were exfoliated into the P-HTO-NS. This reaction revealed that the pore sizes of the P-HTO-NS were the same as those of the P-HTO platelike particles, which corresponded to the sizes of BT nanoparticles in the BT/HTO nanocomposite. Thus, the pore size was controllable by controlling the size of the synthesized BT nanoparticles. Moreover, the BT nanoparticle size in the BT/HTO nanocomposite could be adjusted by the solvothermal reaction conditions, including the reaction solvent, temperature, and Ba/Ti ratio in the reaction system.

3.5 Fabrication of nanoporous HTO nanosheet membrane (M-P-HTO)

The M-P-HTP was fabricated using the P-HTO-NS to demonstrate its potential application. It was reported that the layered titanate nanosheet film could be fabricated by an LBL nanosheet restacking process [48]. However, the operation procedure of the LBL nanosheet restacking process was complicated. In the present study, we designed a smart and efficient process for the fabrication of nanosheet membranes on a porous substrate, as illustrated in Scheme 1A and Fig. 7. In this procedure, the electrolyte solution can pass through the porous PTFE substrate. Subsequently, the cations of electrolyte solution react with negatively charged P-HTO nanosheets, resulting in formation of the nanosheet membrane by restacking P-HTO-NS on the PTFE substrate surface. The restacked P-HTO nanosheets on the PTFE substrate surface blocks the passage of the electrolyte solution through the PTFE substrate to the nanosheet solution,

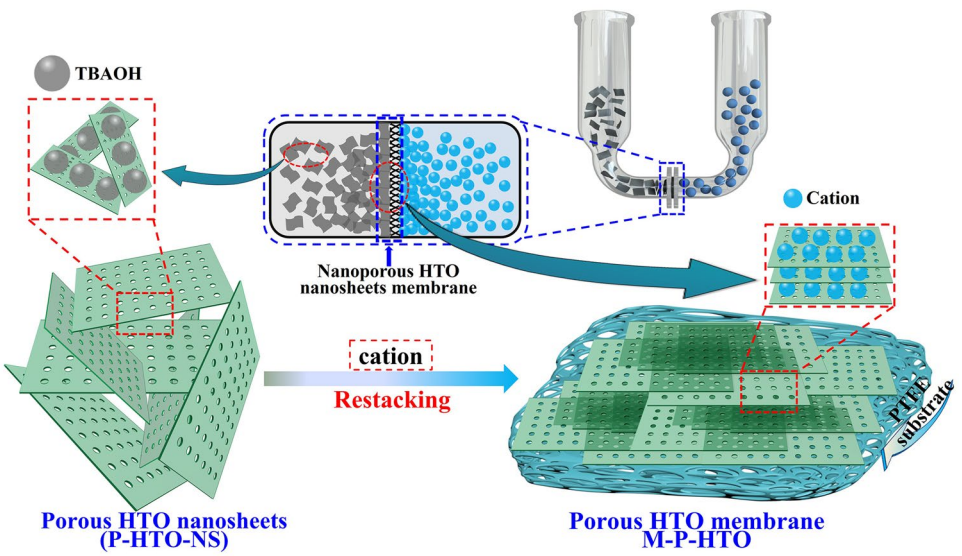

Fig. 7 Schematic illustration of self-adjusting membrane thickness process (SAMTP) for fabrication of M-P-HTO

which terminates the restacking reaction of the nanosheets on the PTFE substrate surface. Thus, during formation process of nanosheet membrane the restacking reaction of the nanosheets occurs mainly on the PTFE substrate surface without the deposited nanosheets where the electrolyte solution can pass through the PTFE substrate. When the PTFE substrate surface was covered completely by the nanosheets, the passing of the electrolyte solution through the PTFE substrate is stopped, resulting ceasing the restacking reaction of the nanosheets. Therefore, the nanosheets are deposited equally on the PTFE substrate surface, and finally, a nanosheet membrane with a uniform thickness can be formed, which is a SAMTP.

To confirm the effectiveness of the SAMTP, first, the M-P-HTO was fabricated by using a non-porous HTO nanosheet solution and electrolyte solutions of HNO_3, $CaCl_2$, and NaCl. A Merck Millipore PTFE membrane substrate was employed as the porous substrate (supporting membrane) due to its high hydrophilicity and chemical stability, as well as its excellent mechanical strength [49]. Figure 8A shows the FE-SEM images of the surfaces of the supporting membrane (Fig. 8A(a)) and the HTO membrane deposited on the supporting membrane using the $CaCl_2$ electrolyte solution (Fig. 8A(b)). After depositing HTO nanosheets on the supporting membrane, a uniform thin film with a thickness of about 50 nm was formed (Fig. S28). A nearly transparent thin film without visible defects is evident in the photograph (inset in Fig. 8A(b)). The supporting membrane exhibited a static water contact angle (WCA) of 50.3°. After depositing the HTO nanosheets on the surface, the WCA decreased to 35.6° due to the excellent hydrophilicity of the HTO nanosheet membrane (Fig. 8B), suggesting an extensive application potential in water treatment [50]. The above results demonstrated the effectiveness of the SAMTP for the fabrication of M-P-HTO on a porous substrate.

To study the influence of the electrolyte solution on the formation of the HTO membrane, various kinds of electrolyte solutions were used to fabricate the HTO membranes. Figure 8C illustrates the dependences of the NaCl permeance on the HTO nanosheet deposition time in the SAMTP for the HTO membranes fabricated using 0.2 mol·L^{-1} $CaCl_2$, 0.2 mol·L^{-1} NaCl and 0.5 mol·L^{-1} HNO_3 solutions. When the HNO_3 solution was used, the NaCl permeance decreased with increasing HTO nanosheet deposition time and reached a constant value after 4 h of deposition, suggesting that almost all the pores of the supporting membrane were covered by HTO nanosheets after deposition treatment. The HTO membranes fabricated using the $CaCl_2$ and NaCl solutions exhibited similar behaviors to those fabricated using the HNO_3 solution. However, the HTO membrane fabricated using the $CaCl_2$ solution exhibited the lowest NaCl permeance, i.e., the highest NaCl rejection performance, of

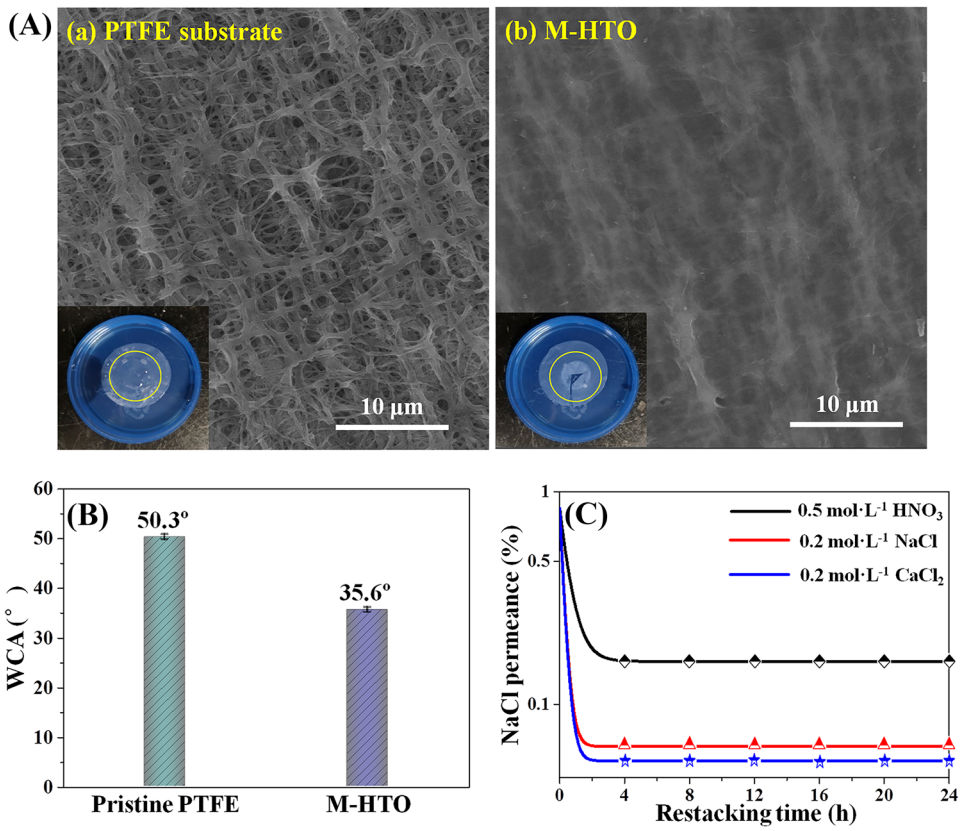

Fig. 8 **A** FE-SEM images of (**a**) polytetrafluoroethylene (PTFE) substrate surface and (**b**) M-HTO membrane surface (inset images are their photographs). **B** Water contact angles (WCAs) of PTFE substrate and M-HTO membrane. **C** Dependence of NaCl permeance on restacking time of non-porous HTO nanosheet membranes fabricated using different electrolyte solutions

the three kinds of electrolyte solutions. This was ascribed to the stronger binding between divalent cations of Ca^{2+} and negatively charged HTO nanosheets in the restacking process of the HTO nanosheets than those of monovalent cations of Na^+ and H^+ in the process of depositing the HTO membrane on the surface of the supporting membrane [51]. Therefore, the optimized conditions for the fabrication of the HTO membrane were 4 h of deposition with a 0.2 mol·L^{-1} $CaCl_2$ solution, which was employed for the subsequent nanosheet membrane fabrication.

The M-P-HTO was fabricated using the nanoporous HTO nanosheets obtained by the SAMTP with a $CaCl_2$ solution. Figure 9a, c, and e show the FE-SEM images and WCAs of the M-P-HTO nanosheet membranes fabricated using the P-HTO-0.5–125-Z nanosheet solution. The fabricated nanoporous membranes possessed an architecture with a uniform thickness without evident cracking, implying that the P-HTO-NS was deposited successfully on the supporting membrane by the SAMTP. The WCAs were 36.2° for the M-P-HTO-0.5–125-W, 34.8° for the M-P-HTO-0.5–125-W/E, and 35.7° for the M-P-HTO-0.5–125-E membranes, which were similar to that of the non-porous HTO nanosheet membrane and smaller than that of the supporting membrane (Fig. 8B). Thus, the M-P-HTO possessed excellent hydrophilicity. Figure 9b, d, and f depict the cross-sectional images of the M-P-HTO-0.5–125-W, M-P-HTO-0.5–125-W/E, and M-P-HTO-0.5–125-E membranes, respectively. The thicknesses of all of the fabricated M-P-HTO membranes were nearly 50 nm, which were the same as those of the non-porous HTO membranes (Fig. S28). The uniform nanometer-scale thickness of M-P-HTO could guarantee a high water permeance and separation performance.

To investigate the porosity and pore size of the M-P-HTO, the rejection efficiencies were evaluated using NaCl, methylene blue (MB), and polydopamine (PD) solutions, as shown in Fig. 10. These solutions contained solutes with different sizes. The solute sizes were about 0.7 nm for Na^+ ions, 1.5 nm for MB molecules, and 100 nm for PD particles, respectively [52, 53]. The average particle size of the PD was evaluated from the particle size distribution, as displayed in Fig. S29. As illustrated in Fig. 10, the non-porous HTO nanosheet membrane (M-HTO, Fig. 10a) exhibited very high rejection efficiencies for PD (> 99%), MB (92%), and NaCl (88%), suggesting that almost all the pores of the supporting membrane were blocked by the non-porous HTO nanosheets. The rejection efficiency decreased slightly in the order of PD > MB > NaCl, which corresponded to the decreasing order of the sizes of the solutes. This result suggested that there were a handful of very small pores in the M-HTO.

The pore size of the M-P-HTO corresponded to the pore size of P-HTO-NS used in the membrane fabrication process. The M-P-HTO-0.5–125-E membrane possessed the smallest pore size (Fig. 10b). PD could not pass through the pores, and only a small amount of MB could pass through. However, the small ions of the NaCl solution could pass through the pores. The rejection efficiencies for PD, MB, and NaCl were 95%, 82%, and 67% at 12 h, respectively. Only a small amount of PD could pass through the M-P-HTO-0.5–125-W and M-P-HTO-0.5–125-W/E membranes. However, MB and NaCl could pass through these

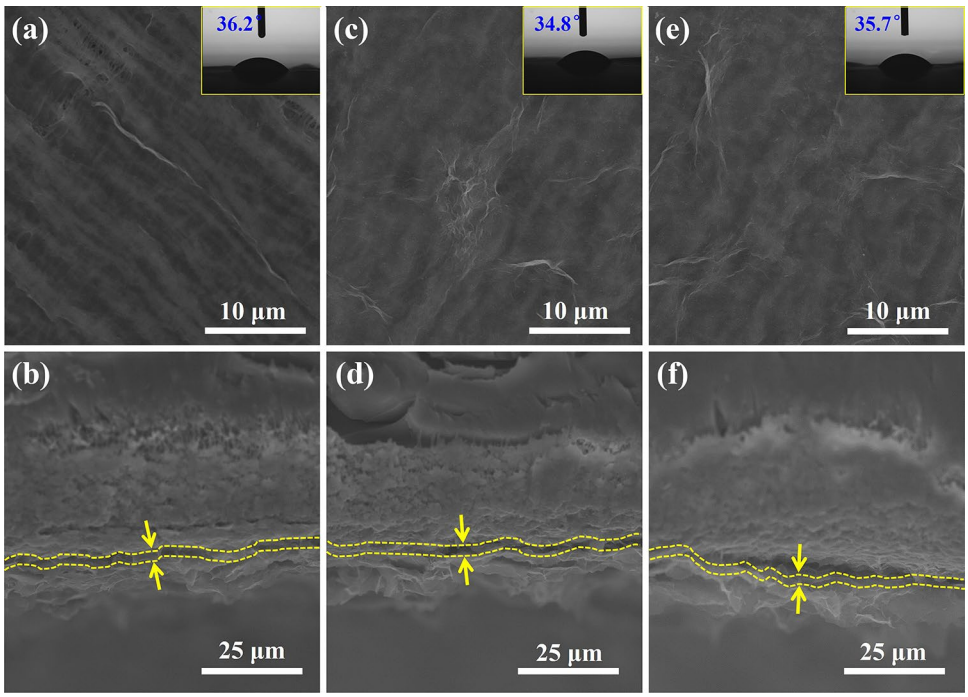

Fig. 9 FE-SEM images of **a**, **c**, **e** surfaces and **b**, **d**, **f** cross-sections of **a**, **b** M-P-HTO-0.5–125-W, **c**, **d** M-P-HTO-0.5–125-W/E, and **e**, **f** M-P-HTO-0.5–125-E membranes. The corresponding WCAs are shown in insets of surface images

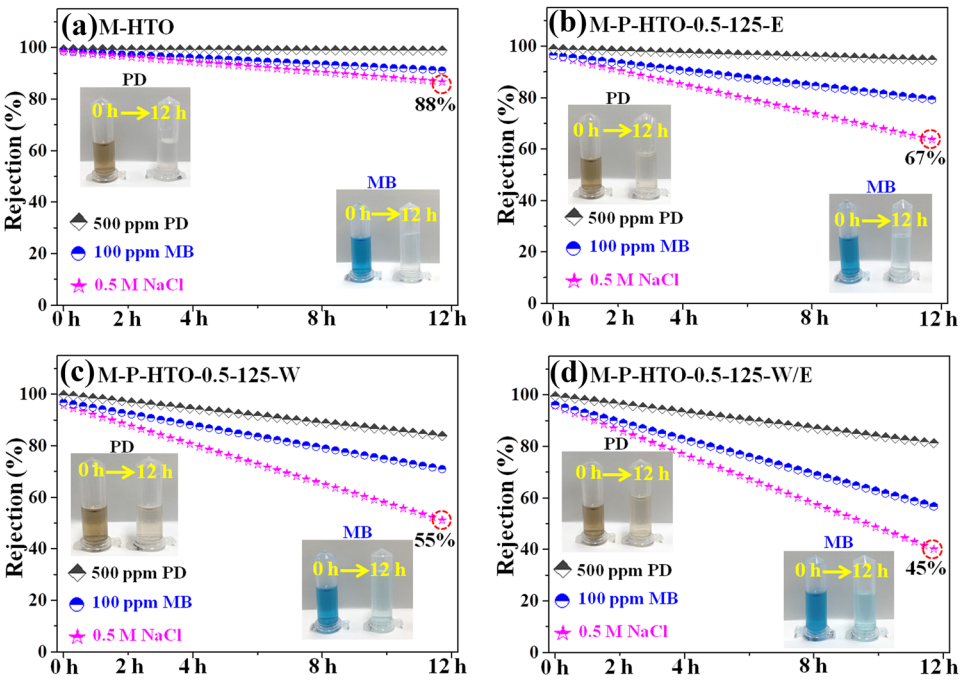

Fig. 10 NaCl, methylene blue (MB), and polydopamine (PD) rejection performances and time-course photographs of PD and MB solutions for **a** non-porous M-HTO, **b** M-P-HTO-0.5–125-E, **c** M-P-HTO-0.5–125-W, and **d** M-P-HTO-0.5–125-W/E membranes

two kinds of nanoporous membranes. At 12 h, the rejection efficiencies for PD, MB, and NaCl were 83%, 72%, and 55% for M-P-HTO-0.5–125-W (Fig. 10c), respectively, and the corresponding values for M-P-HTO-0.5–125-W/E were 81%, 60%, and 45% (Fig. 10d). The rejection results revealed that the pore sizes of the nanoporous membranes were in the order of M-P-HTO-0.5–125-E < M-P-HTO-0.5–125-W < M-P-HTO-0.5–125-W/E. The pore size of M-P-HTO-0.5–125-E was close to the size of MB (1.5 nm). The pore sizes of the M-P-HTO-0.5–125-W and M-P-HTO-0.5–125-W/E nanocomposites were larger than MB (1.5 nm) but smaller than PD (100 nm). Notably, the pore size of the M-P-HTO exhibited a clear dependence on the pore size of the P-HTO-NS, which corresponded to the BT particle size in the BT/HTO nanocomposite. Thus, the pore size could be controlled by the solvothermal synthesis conditions of the BT/HTO nanocomposite. Furthermore, the results also reveal that the uniform M-P-HTO could be fabricated by the SAMTP. In this process, the pore sizes of the nanoporous nanosheets were inherited by the nanoporous membranes.

We also explored the water-transport properties of the fabricated HTO and nanoporous HTO membranes by the measurement of the water permeance capacities of NaCl, MB, and PD solutions, and the results are shown in Fig. S30. After deposition of the non-porous HTO nanosheet on the supporting membrane, the water flux through the membrane decreased from 8.4 to 6.4 L/m^2·h for the NaCl solution. The water fluxes of the nanoporous HTO nanosheet membranes were in the order of M-P-HTO-0.5–125-W/E (7.8 L/m^2·h) > M-P-HTO-0.5–125-W (7.3 L/m^2·h) > M-P-HTO-0.5–125-E (6.7 L/m^2·h) for NaCl solution, which were larger than those of the non-porous HTO nanosheet membrane (6.4 L/m^2·h) but smaller than those of the supporting membrane (8.4 L/m^2·h), indicating that the nanoporous HTO nanosheets possessed larger water permeance than those of the non-porous HTO nanosheets. The water fluxes for the MB and PD solutions were in the same order for NaCl solution: M-P-HTO-0.5–125-W/E > M-P-HTO-0.5–125-W > M-P-HTO-0.5–125-E > M-HTO, which was consistent with the aperture rate of the nanoporous HTO nanosheets.

The solute size also affected the water flux, where the water flux decreased with increasing solute size for all these nanoporous HTO nanosheet membranes. Apparently, the large solute molecules or ions inhibited the water molecules from passing through the nanopores of the nanosheet membranes. The above results further revealed that the nanoporous HTO nanosheet membranes exhibited excellent water permeance owing to their high hydrophilicity. Moreover, the water flux was dependent on the aperture rates of the nanoporous HTO nanosheets, which could be controlled by the solvothermal synthesis conditions of the BT/HTO nanocomposite.

The durability of the nanoporous HTO nanosheet membranes was also evaluated because durability is essential for their application as filtration materials. The FE-SEM images of the nanoporous HTO nanosheet membranes after rejection and water flux measurements revealed that no cracks or re-exfoliation were evident on the surfaces of the nanosheet membranes (Fig. S31), demonstrating that the nanosheet membranes with excellent mechanical strength and good durability could be fabricated using the SAMTP proposed in this work.

4 Conclusions

The study demonstrated a soft chemical solvothermal process for preparing nanoporous HTO platelike nanoparticles. Nanoporous HTO nanosheets with uniform pore sizes were prepared by exfoliation of the nanoporous HTO particles. A self-adjusting membrane thickness process (SAMTP) was designed to fabricate inorganic nanoporous membranes. The nanoporous HTO membranes fabricated by the SAMTP possessed uniform self-adjusted thicknesses, excellent hydrophilicity, high water fluxes, and good durability. The fabricated nanoporous HTO nanosheet membranes feature a high water permeance and good selectivity for separating solutes with different size due to the high intrinsic hydrophilicity of the inorganic titanate nanosheets and the facilely controlled pore size in the membranes. In addition, this convenient and low-cost inorganic membrane fabrication technique could also be applied to other nanosheet membranes. Therefore, this work would broaden the strategic vision for the fabrication of inorganic nanosheet membranes, which could provide an excellent candidate for efficient water treatment and small-molecule separation. Besides, we are still committed to optimize the solvothermal reaction conditions and investigate membrane fabrication technique to improve the membrane performance in our future study.

Supplementary Information The online version contains supplementary material available at https://doi.org/10.1007/s42114-022-00579-z.

Author contribution Fangyi Yao: experimentations, conceptualization, methodology, formal analysis, investigation, data curation, writing—original draft. Wenxiong Zhang, Dengwei Hu, Sen Li and Xingang Kong: methodology, formal analysis. Shinobu Uemura and Takafumi Kusunose: supervision and data discussions. Qi Feng: conceptualization, writing—review and editing, supervision, project administration.

Funding This work was supported by The Grants-in-Aid for Scientific Research (C) (No. 21K04832) from Japan Society for the Promotion of Science.

Data availability The datasets generated during and/or analysed during the current study are available from the corresponding author on reasonable request.

Declarations

Conflict of interest The authors declare no competing interests.

References

1. Schlosser CA, Strzepek K, Gao X, Fant C, Blanc É, Paltsev S, Jacoby H, Reilly J, Gueneau A (2014) The future of global water stress: an integrated assessment. Earths Future 2:341–361
2. Gao M, Zhu L, Peh CK, Ho GW (2019) Solar absorber material and system designs for photothermal water vaporization towards clean water and energy production. Energy Environ Sci 12:841–864
3. Zhang J, Liu L, Si Y, Yu J, Ding B (2020) Electrospun nanofibrous membranes: an effective arsenal for the purification of emulsified oily wastewater. Adv Funct Mater 30:2002192
4. Mastropietro TF, Bruno R, Pardo E, Armentano D (2021) Reverse osmosis and nanofiltration membranes for highly efficient PFASs removal: overview, challenges and future perspectives. Dalton Trans 50:5398–5410
5. Radha B, Esfandiar A, Wang F, Rooney AP, Gopinadhan K, Keerthi A, Mishchenko A, Janardanan A, Blake P, Fumagalli L-H, Garaj S, Haigh SJ, Grigorieva IV, Wu HA, Geim AK (2016) Molecular transport through capillaries made with atomic-scale precision. Nature 538:222–225
6. Fane AG, Wang R, Hu MX (2015) Synthetic membranes for water purification: status and future. Ange Chem Int Ed 54:3368–3386
7. Striemer CC, Gaborski TR, McGrath JL, Fauchet PM (2007) Charge-and size-based separation of macromolecules using ultrathin silicon membranes. Nature 445:749–753
8. Dong F, Pang Z, Yang S, Lin Q, Song S, Li C, Song S, Li C, Ma XY, Nie S (2022) Improving wastewater treatment by triboelectric-photo/electric coupling effect. ACS Nano 16:3449–3475
9. Zhao F, Guo Y, Zhou X, Shi W, Yu G (2020) Materials for solar-powered water evaporation. Nat Rev Mater 5:388–401
10. Belfort G (2019) Membrane filtration with liquids: a global approach with prior successes, new developments and unresolved challenges. Angew Chem Int Ed 131:1908–1918
11. Voutchkov N (2018) Energy use for membrane seawater desalination-current status and trends. Desalination 431:2–14
12. Zhang Y, Ruan H, Guo C, Liao J, Shen J, Gao C (2020) Thin-film nanocomposite reverse osmosis membranes with enhanced antibacterial resistance by incorporating p-aminophenol-modified graphene oxide. Sep Purif Technol 234:116017
13. Zhao S, Liao Z, Fane A, Li J, Tang C, Zheng C, Lin J, Kong L (2021) Engineering antifouling reverse osmosis membranes: a review. Desalination 499:114857
14. Ng LY, Mohammad AW, Leo CP, Hilal N (2013) Polymeric membranes incorporated with metal/metal oxide nanoparticles: a comprehensive review. Desalination 308:15–33
15. Heiranian M, Farimani AB, Aluru NR (2015) Water desalination with a single-layer MoS2 nanopore. Nat commun 6:1–6
16. Echaide-Górriz C, Navarro M, Téllez C, Coronas J (2017) Simultaneous use of MOFs MIL-101(Cr) and ZIF-11 in thin film nanocomposite membranes for organic solvent nanofiltration. Dalton Trans 46:6244–6252
17. Bhanja P, Na J, Jing T, Lin J, Wakihara T, Bhaumik A, Yamauchi Y (2019) Nanoarchitectured metal phosphates and phosphonates: a new material horizon toward emerging applications. Chem Mater 31:5343–5362
18. Goh PS, Ismail AF (2018) A review on inorganic membranes for desalination and wastewater treatment. Desalination 434:60–80
19. Liu GP, Jin WQ, Xu NP (2015) Graphene-based membranes. Chem Soc Rev 44:5016–5030
20. Kar S, Bindal RC, Tewari PK (2012) Carbon nanotube membranes for desalination and water purification: challenges and opportunities. Nano Today 7:385–389
21. Kunduru KR, Nazarkovsky M, Farah S, Pawar RP, Basu A, Domb AJ (2017) 2- Nanotechnology for water purification: applications of nanotechnology methods in wastewater treatment. Water Purif 33–74
22. Liu Y, Ban YJ, Yang WS (2017) Microstructural engineering and architectural design of metal-rganic framework membranes. Adv Mater 29:1606949
23. Sun PZ, Wang KL, Zhu HW (2016) Recent developments in graphene-based membranes: structure, mass-transport mechanism and potential applications. Adv Mater 28:2287–2310
24. Yang Y, Yang XD, Liang L, Gao Y, Cheng HY, Li XM, Zou MC, Ma R, Yuan Q, Duan XF (2019) Large-area

graphene-nanomesh/carbon-nanotube hybrid membranes for ionic and molecular nanofiltration. Science 364:1057–1062
25. Koh DY, Lively RP (2015) Membranes at the limit. Nat Nanotechnol 10:385–386
26. Pakulski D, Czepa W, Buffa SD, Ciesielski A, Samorì P (2020) Atom-thick membranes for water purification and blue energy harvesting. Adv Funct Mater 30:1902394
27. Koenig SP, Wang L, Pellegrino J, Bunch JS (2012) Selective molecular sieving through porous graphene. Nat Nanotechno 7:728–732
28. Surwade SP, Smirnov SN, Vlassiouk IV, Unocic RR, Veith GM, Dai S, Mahurin SM (2015) Water desalination using nanoporous single-layer graphene. Nat Nanotechnol 10:459–464
29. Hu M, Mi BX (2013) Enabling graphene oxide nanosheets as water separation membranes. Sci Technol 47:3715–3723
30. Wei Y, Zhang YS, Gao XL, Ma Z, Wang XJ, Gao CJ (2018) Multilayered graphene oxide membranes for water treatment: a review. Carbon 139:964–981
31. Joshi RK, Carbone P, Wang FC, Kravets VG, Su Y, Grigorieva IV, Wu HA, Geim AK, Nair RR (2014) Precise and ultrafast molecular sieving through graphene oxide membranes. Science 343:752–754
32. Liang YZ, Zhu YZ, Liu C, Lee KR, Hung WS, Wang ZY, Li YY, Elimelich M, Jin J, Lin SH (2020) Polyamide nanofiltration membrane with highly uniform sub-nanometre pores for sub-1 Å precision separation. Nat Commun 11:1–9
33. Sun M, Li JH (2018) Graphene oxide membranes: Functional structures, preparation and environmental applications. Nano Today 20:121–137
34. Chen C, Wang JM, Liu D, Yang C, Liu YC, Ruoff RS, Lei WW (2018) Functionalized boron nitride membranes with ultrafast solvent transport performance for molecular separation. Nat Commun 9:1–8
35. Shikha S, Salafi T, Cheng JT, Zhang Y (2017) Versatile design and synthesis of nano-arcodes. Chem Soc Rev 46:7054–7093
36. Shin MG, Kwon SJ, Park H, Park YI, Lee JH (2020) High-performance and acid-resistant nanofiltration membranes prepared by solvent activation on polyamide reverse osmosis membranes. J Memb Sci 595:117590
37. Rodriguez PG, Lubbers R, Veldhuis SA, Narygina O, Lette W, Schipper DJ, ten Elshof JE (2017) Tuning the structure and ionic interactions in a thermochemically stable hybrid layered titanate-based nanocomposite for high temperature solid lubrication. Adv Mater Interfaces 4:1700047
38. Wen PH, ItoH TWP, Feng Q (2007) Single nanocrystals of anatase-type TiO2 prepared from layered titanate nanosheets: formation mechanism and characterization of surface properties. Langmuir 23:11782–11790
39. Baek CC, Yun JH, Wang HS, Wang JE, Park H, Park KI, Kim DK (2018) Enhanced output performance of a lead-free nanocomposite generator using BaTiO3 nanoparticles and nanowires filler. Appl Surf Sci 429:1644–2170
40. Zhu CQ, Cai ZM, Guo LM, Li LT, Wang XH (2021) Grain size engineered high-performance nanograined BaTiO3-based ceramics: experimental and numerical prediction. J Am Ceram Soc 104:273–283
41. Hu DW, Ma H, Tanaka Y, Zhao LF, Feng Q (2015) Ferroelectric mesocrystalline BaTiO3/SrTiO3 nanocomposites with enhanced dielectric and piezoelectric responses. Chem Mater 27:4983–4994
42. Hu DW, Miao L, Zhang Z, Li LJ, Wang Y, Cheng HL, Sewvandi GA, Feng Q, Fan MJ, Zhao LF (2018) One-dimensional piezoelectric BaTiO3 polycrystal of topochemical mesocrystal conversion from layered H2Ti4O9·H2O single crystal. Cryst Growth Des 18:7264–7274
43. Zhang WX, Li S, Ma H, Hu DW, Kong XG, Uemura S, Kusunose T, Feng Q (2019) Ferroelectric mesocrystalline BaTiO3/BaBi4Ti4O15 nanocomposite: formation mechanism, nanostructure, and anomalous ferroelectric response. Nanoscale 11:3837–3846
44. Sun QM, Gu QL, Zhu KJ, Jin RY, Liu J, Wang SJ, Qiu JH (2017) Crystalline structure, defect chemistry and room temperature colossal permittivity of Nd-doped barium titanate. Sci Rep 7:1–8
45. Chen CD, Sewvandi GA, Kusunose T, Tanaka Y, Nakanishi S, Feng Q (2014) Synthesis of {010}-faceted anatase TiO2 nanoparticles from layered titanate for dye-sensitized solar cells. CrystEngComm 16:8885–8895
46. Feng Q, Hirasawa M, Kajiyoshi K, Yanagisawa K (2007) Hydrothermal soft chemical synthesis of BaTiO3 and titanium oxide with cocoon-like particle morphology. J Mater Sci 42:640–645
47. Zhang WX, Ma H, Li S, Hu DW, Kong XG, Uemura S, Kusunose T, Feng Q (2018) Anomalous piezoelectric response of ferroelectric mesocrystalline BaTiO3/Bi0.5Na0.5TiO3 nanocomposites designed by strain engineering. Nanoscale 10:8196–8206
48. Ying YP, Tong MM, Ning SC, Ravi SK, Peh SB, Tan SC, Pennycook SJ, Zhao D (2020) Ultrathin two-dimensional membranes assembled by ionic covalent organic nanosheets with reduced apertures for gas separation. J Am Chem Soc 142:4472–4480
49. Benipal N, Qi J, Gentile JC, Li WZ (2017) Direct glycerol fuel cell with polytetrafluoroethylene (PTFE) thin film separator. Renew Energ 105:647–655
50. Ren J, Li JF, Xu ZZ, Liu Y, Cheng FQ (2020) Simultaneous antifouling and flux-enhanced membrane distillation via incorporating graphene oxide on PTFE membrane for coking wastewater treatment. Appl Surf Sci 531:147349
51. Fang LF, Zhou MY, Cheng L, Zhu BK, Matsuyama H, Zhao S (2019) Positively charged nanofiltration membrane based on cross–linked polyvinyl chloride copolymer. J Membrane Sci 572:28–37
52. Fu JW, Chen ZH, Wang MH, Liu SJ, Zhang JH, Zhang JN, Han RP, Xu Q (2015) Adsorption of methylene blue by a high-efficiency adsorbent. Chem Eng J 259:53–61
53. Bastús NG, MerkoçI F, Piella J, Puntes V (2014) Synthesis of highly monodisperse citrate-stabilized silver nanoparticles of up to 200 nm: kinetic control and catalytic properties. Chem Mater 26:2836–2846